

SPARC: Spine with Prismatic and Revolute Compliance for Quadruped Robots

Yue Wang¹

Abstract—We present SPARC, a compact, open-source 3-DoF sagittal-plane spine module that combines revolute (pitch) and prismatic (axial) motion with programmable task-space impedance for quadruped robots. The system integrates three torque-controlled actuators, a 1 kHz control board, and protected power electronics in a 1.26 kg package. A floating-base impedance controller with dynamics compensation renders tunable spring-damper behavior along horizontal, vertical, and rotational axes. Benchtop experiments validate the approach: quasi-static tests demonstrate linear force-displacement characteristics with commanded horizontal stiffness spanning 300–700 N/m ($\leq 1.5\%$ error, $R^2 \geq 0.992$), while dynamic trials confirm predictable damping behavior across multiple settings. Furthermore, simulation studies reveal that adapting spine stiffness based on terrain slope and stride length significantly reduces the cost of transport. SPARC provides an open-source platform for systematic studies of spine compliance in legged locomotion, with complete hardware and firmware resources available for community use. Github repository: <https://github.com/YueWang996/sparc.git>

I. INTRODUCTION

Quadruped mammals use flexible spines to lengthen stride, absorb landing impacts, and generate thrust, achieving agility and efficiency [1] beyond what rigid torsos can provide [2]. Research indicates that quadruped animals actively modulate spinal kinematics across speeds to optimize locomotion, utilizing spinal flexion to enhance stride length and elastic energy storage [3], [4]. Most robotic quadrupeds, however, employ rigid trunks to simplify structure and control [5], [6], which constrains energy shaping and workspace modulation at high speed. We bridge this gap by developing a compact spine capable of both sagittal-plane bending and axial extension under active control, with continuously tunable compliance.

Existing robotic spine designs fall into three categories, each with distinct limitations. *Passive compliant spines* use fixed elastic elements that provide energy storage but cannot adapt stiffness to varying task demands [7]. *Actuated position-controlled spines* offer adjustable postures but behave as effectively rigid structures during stance, limiting their energy efficiency benefits [8]. *Spring-loaded release mechanisms* can generate powerful axial thrusts but require manual pre-compression and operate open-loop, making them unsuitable for continuous gait cycles [9]. In contrast, biological spines exhibit loosely coupled vertebrae that enable

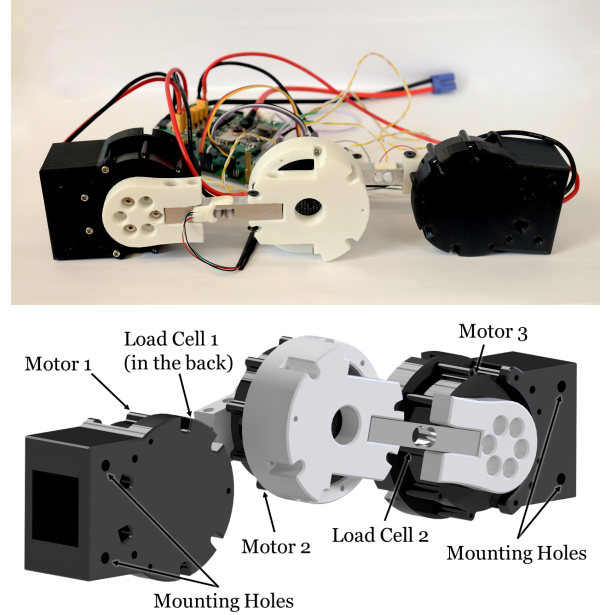


Fig. 1: The compact SPARC system. It is designed to mount between the fore and hind body segments of a quadruped robot. Top: assembled prototype used in experiments. Bottom: structure of the spine unit.

simultaneous bending and axial compression—coupled revolute and prismatic motions that attenuate landing impacts and generate propulsive forces [10]. This bio-inspired compliance improves locomotion efficiency [11], yet no existing robotic system combines closed-loop control of both revolute and prismatic degrees of freedom with programmable impedance.

To address this gap, we present **SPARC** (**S**pine with **P**rismatic **A**nd **R**evolute **C**ompliance, as shown in Figure 1), a compact, open-source 3-DoF sagittal-plane spine module designed to mount between fore and hind body segments. The main contributions of this paper are:

- 1) We design and fabricate a spine integrating three torque-controlled actuators, a motion control board with 1 kHz bandwidth, and a protected power unit in a 1.26 kg package, achieving simultaneous prismatic and revolute motion.
- 2) We develop a task-space impedance control law and incorporate a smooth Stribeck friction compensation, rendering programmable spring-damper behavior without explicit inertia shaping.
- 3) We validate the system through benchtop characterization (300–700 N/m stiffness range) and simulation studies, demonstrating how spine compliance opti-

¹Yue Wang is with the School of ECS, University of Southampton, United Kingdom. Yue.Wang@soton.ac.uk.

*This work is supported by the School of Electronic and Computer Science (ECS), University of Southampton.

mization reduces the cost of transport across varying slopes and stride lengths.

The remainder of this paper is organized as follows. Section II reviews spine mechanisms and control approaches and highlights gaps in prismatic motion. Section III details SPARC hardware and control, followed by experiments and analysis in Section IV. Section V concludes with limitations and future work.

II. RELATED WORK

Biological quadrupeds achieve remarkable agility through flexible spines that can simultaneously bend and compress. This coupling of revolute and prismatic motion serves distinct functional roles. During galloping, for instance, canine vertebrae flex in the sagittal plane to extend stride length during flight and compress axially to absorb landing impacts [10]. This mechanical coupling improves locomotion efficiency and amplifies power output [11], [1]. Robotics has struggled to replicate this capability. Existing approaches are short on combining closed-loop prismatic motion with tunable compliance.

A. Robotic spine design

Most robotic spines focus on revolute motion. Early bio-inspired designs introduced bending motion on sagittal plane to extend leg workspace [13] and improve gait efficiency [8]. More recent work explores pitch-yaw coordination for turning agility [14] and roll-axis twisting for lateral maneuvers [15]. These revolute-only architectures deliver measurable benefits: torso-leg phase coordination, enlarged workspace, and improved maneuverability. However, they fundamentally lack the axial degree of freedom observed in biological systems. Without prismatic motion, robotic spines cannot modulate effective body length during flight or absorb landing impacts through controlled compression. This constraint limits their ability to replicate the functional repertoire of mammalian spines.

Prismatic motion in robotic spines is still rare and elementary. [9] developed a spring-loaded lockable mechanism that can be manually pre-compressed and locked at different lengths to provide tunable passive compliance. They demonstrated this system in vertical jumping and landing experiments, where the compliant spine absorbed landing impacts effectively through axial compression and energy dissipation. However, this design requires manual pre-loading before each action and is demonstrated only for discrete maneuvers rather than continuous periodic gaits. The spine must be reset between jumping attempts, making it suitable for one-off explosive movements but not for sustained locomotion cycles like trotting or galloping. Simulation studies suggest that closed-loop axial compliance could improve stability [17] and the ability of rapid acceleration and deceleration [16], but experimental validation of continuously controllable, feedback-controlled prismatic motion in hardware remains absent from the literature.

B. Realization of Compliance

The manner in which compliance is realized strongly affects functional capability. Early passive designs embed springs or elastomers directly in the spine structure [7]. These provide energy storage and return but have fixed mechanical properties that cannot adapt across tasks or gait phases. Mechanically variable stiffness (MVS) mechanisms address this limitation and enable stiffness adjustment through parameter changes (e.g., spring preload [12], [11], [18]). However, these systems operate at low bandwidth and add mechanical complexity.

The advent of quasi-direct-drive (QDD) actuators has enabled a third paradigm: joint-level torque control that renders virtual spring-damper behavior at each actuator through the leg PD controller. This approach provides high-bandwidth impedance tuning and is now common in state-of-the-art legged robots [19], [20]. However, when each spine joint is controlled independently, the resulting compliance is defined in joint space rather than task space. Even with different stiffness values at each joint, the system cannot directly specify anisotropic stiffness in Cartesian coordinates. During trotting, for example, a dog’s spine exhibits high vertical stiffness to support body weight while maintaining lower horizontal stiffness for stride modulation [10]. Achieving such axis-selective compliance requires coordinated task-space impedance control that maps desired Cartesian stiffness (e.g., along x , z , and θ) to joint torques through the system Jacobian. Without this coordination, joint-level control couples task-space directions through the kinematic structure, preventing independent shaping of horizontal, vertical, and rotational compliance.

As summarized in Table I, no existing spine supports revolute and prismatic motion with real-time tunable, axis-selective compliance under continuous closed-loop control. SPARC addresses this gap by coordinating three torque-controlled actuators to enable independent specification of stiffness and damping along horizontal, vertical, and rotational axes.

III. METHODOLOGY

This section details the hardware design and control of SPARC, as well as a method for integrating SPARC into a quadruped platform.

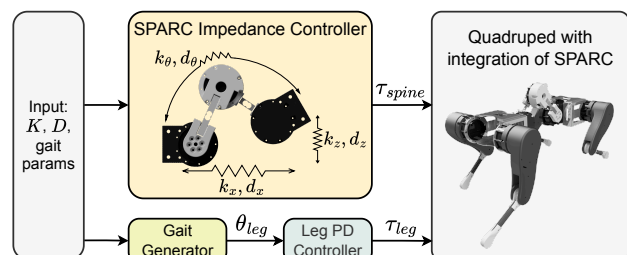


Fig. 2: Control architecture for SPARC integration with a quadruped robot.

A. Hardware Design

SPARC is a self-contained module with three main components: a 3-DoF active spine, a Motion Control Board (MCB), and a Power Management Unit (PMU). The active spine provides sagittal-plane motion through three quasi-direct-drive actuators (Xiaomi Cybergear, 12 N·m peak torque each) that enable high-bandwidth torque control. Lightweight 3D-printed links concentrate 75% of the mass at the actuators to minimize reflected inertia. Two load cells on the central links provide torque feedback. The MCB runs a 1 kHz control loop on an STM32F405 microcontroller and communicates with all three actuators over a single CAN bus. An onboard IMU provides attitude estimation. The PMU supplies power with over-current and thermal protection, accepting either a 6S LiPo battery or 24 V bench supply.

To validate the design, SPARC connects the front and hind bodies of a custom 8-DoF quadruped through reserved mounting holes (Fig. 2). Locomotion is achieved via a bounding gait scheduler that generates joint angles for the legs, tracked by a PD controller. This architecture allows users to vary spine parameters (e.g., stiffness and damping) alongside gait settings (frequency, stride, step height) to evaluate performance across different tasks.

B. Impedance Control of SPARC

To render the spine as a compliant, spring-like mechanism, we developed an impedance controller that computes motor torques in real time using a dynamic model. We model SPARC as part of a floating-base system operating in the sagittal plane. The task-space state $x = [x, z, \theta]^\top \in \mathbb{R}^3$ represents the end-effector pose (horizontal position, vertical position, pitch angle) relative to the base link. The full system has generalized coordinates $q \in \mathbb{R}^{10}$ (7 for floating base q_{base} including position and orientation, 3 for spine actuators q_s) and velocities $v \in \mathbb{R}^9$ (6 for base spatial velocity, 3 for spine joint velocities v_s).

The equations of motion for the floating-base system are

$$M(q)\dot{v} + h(q, v) = \tau + J^\top F_{\text{ext}}, \quad (1)$$

where $M(q) \in \mathbb{R}^{9 \times 9}$ is the mass matrix, $h(q, v) = C(q, v) + g(q)$ collects Coriolis and gravity effects, and $\tau \in \mathbb{R}^9$ are the generalized torques acting in direction of generalized

coordinates. Rather than deriving these terms analytically, we compute $M(q)$ using the Composite Rigid Body Algorithm (CRBA) and $h(q, v)$ using the Recursive Newton–Euler Algorithm (RNEA) [21].

The full system mass matrix $M(q)$ partitions into blocks corresponding to base and spine coordinates:

$$M(q) = \begin{bmatrix} M_{bb}(q) & M_{bs}(q) \\ M_{sb}(q) & M_{ss}(q) \end{bmatrix}, \quad (2)$$

where $M_{bb} \in \mathbb{R}^{6 \times 6}$ is the base inertia block, $M_{ss} \in \mathbb{R}^{3 \times 3}$ is the spine inertia block, and $M_{sb} = M_{bs}^\top \in \mathbb{R}^{3 \times 6}$ captures inertial coupling between base and spine motion. Similarly, the nonlinear terms partition as $h(q, v) = [h_b^\top, h_s^\top]^\top$ where $h_s \in \mathbb{R}^3$ contains Coriolis and gravity effects on the spine joints.

Extracting the spine dynamics yields:

$$M_{sb}(q)\dot{v}_{\text{base}} + M_{ss}(q)\dot{v}_s + h_s(q, v) = \tau_s + J_s^\top F_{\text{ext}}. \quad (3)$$

For the SPARC experiments in this paper, the base is mechanically fixed such that $\dot{v}_{\text{base}} = 0$, therefore, we simplify the dynamics to:

$$M_{ss}(q)\dot{v}_s + h_s(q, v) = \tau_s + J_s^\top F_{\text{ext}}, \quad (4)$$

where $\tau_s \in \mathbb{R}^3$ are the spine joint torques. For on-robot deployment, the coupling term $M_{sb}\dot{v}_{\text{base}}$ could be compensated using IMU-based acceleration estimates. However, our quadruped locomotion simulation suggests that the natural compliance of the impedance controller is sufficient to handle this coupling as an external disturbance without explicit compensation, avoiding the need for potentially noisy acceleration feedforward.

The control objective is to render a mass–spring–damper interaction in task space,

$$\Lambda(x)\ddot{\tilde{x}} + D\dot{\tilde{x}} + K\tilde{x} = -F_{\text{ext}}, \quad (5)$$

where $\tilde{x} = x_d - x$ is the task-space error (i.e. the displacement of the spring), and

$$\Lambda(x) = (J_s(q)M_{ss}^{-1}(q)J_s^\top(q))^{-1}$$

is the task-space inertia matrix. The task-space Jacobian $J_s(q) \in \mathbb{R}^{3 \times 3}$ maps spine joint velocities to task-space velocities of the end-effector relative to the base link. Diagonal

TABLE I: Comparison of spine designs in quadruped robots. SPARC is the first to combine revolute and prismatic motion with real-time tunable, axis-selective compliance under continuous closed-loop control.

Work	Revolute Motion	Prismatic Motion	Control Type	Real-time Tunable	Axis-selective Compliance	Key Capability
[12]	✓	✗	Passive elastic	✗	✗	Gait modulation
[8]	✓	✗	Position	✗	✗	Modest efficiency gains
[13]	✓	✗	Joint torque	✗	✗	Extended workspace
[14]	✓	✗	Joint torque (MPC)	✗	✗	Load distribution
[11]	✓	✗	Variable stiffness	✓	✗	Adjustable compliance
[15]	✓	✗	Joint torque	✗	✗	Turning agility
[9]	✗	✓	Lockable spring	✗	✗	Impact absorption
[16]	✗	✓	Simulation only	—	—	Acceleration study
[17]	✗	✓	Simulation only	—	—	Long jump performance
SPARC (this work)	✓	✓	Task-space impedance	✓	✓	Tunable anisotropic compliance

stiffness and damping matrices are used:

$$K = \text{diag}(k_x, k_z, k_\theta), \quad D = \text{diag}(d_x, d_z, d_\theta).$$

To achieve this behavior, the impedance control law is defined:

$$\begin{aligned} F_{\text{imp}} &= K\tilde{x} + D\dot{\tilde{x}}, \\ F_{\text{comp}} &= \Lambda(x)\dot{J}_s(q, v)v_s, \\ \tau_s &= h_s(q, v) + J_s^\top(q)(F_{\text{imp}} - F_{\text{comp}}), \end{aligned} \quad (6)$$

where the task-space impedance force F_{imp} provides the desired spring-damper restoring force, and the compensation force F_{comp} cancels bias acceleration arising from $\dot{J}_s v_s$ in the kinematic acceleration $\ddot{x} = J_s \dot{v}_s + \dot{J}_s v_s$. The term h_s compensates for Coriolis and gravity effects in joint space. Substituting (6) into the spine dynamics and projecting to task space yields the desired closed-loop behavior (5).

To compute Λ , we first solve $(M_{ss} + \varepsilon_1 I)X = J_s^\top$ for $X \in \mathbb{R}^{3 \times 3}$, and form the matrix $A = J_s X \approx J_s M_{ss}^{-1} J_s^\top$. We then obtain the task space inertia matrix Λ by solving the regularized system $(A + \varepsilon_2 I)\Lambda = I$, where $\varepsilon_{1,2}$ are regularization terms ensuring numerical stability. Note that because the external force F_{ext} is not measured, the controller preserves the natural, non-diagonal task-space inertia $\Lambda(x)$ rather than shaping it to a diagonal target. This results in minor inertial coupling between task axes (e.g., an impact in x inducing acceleration in z). While strictly shaping the inertia of the system via the external force F_{ext} feedback [22], adding a force sensor to the end effector is impractical in such a compact module. Furthermore, for the intended locomotion applications, these inertial coupling effects are negligible compared to the compliant behavior enforced by the diagonal stiffness and damping matrices K and D .

To further improve tracking on hardware, the commanded torque is augmented with a smooth Stribeck friction model [23] applied at each joint,

$$\begin{aligned} \tau_{\text{friction}} &= \left(\tau_{\text{kinetic}} + (\tau_{\text{static}} - \tau_{\text{kinetic}}) \exp(-(|v_s|/|v_{\text{st}}|)^\alpha) \right) \\ &\quad \cdot \tanh(\beta v_s) + b v_s, \end{aligned} \quad (7)$$

where τ_{kinetic} and τ_{static} denote Coulomb and static friction, respectively. The parameter b is the viscous coefficient, v_{st} is the Stribeck velocity, and $\alpha, \beta > 0$ are shape parameters. The variable v_s represents the spine joint velocity. This smooth approximation avoids chatter near zero velocity while capturing frictional effects at low speed.

C. Software and Real-Time Implementation

The control software is written in C and runs on the MCB's STM32F405 (@168 MHz) under FreeRTOS, which schedules a 1 kHz high-priority control task. Each cycle computes forward kinematics and the task-space Jacobian J_s , evaluates the full-system mass matrix $M(q)$ and nonlinear terms $h(q, v)$ via RNEA, extracts the spine blocks M_s and h_s , computes the impedance control law (6) with friction compensation (7), and transmits joint torque commands to the three actuators over CAN. Computationally intensive

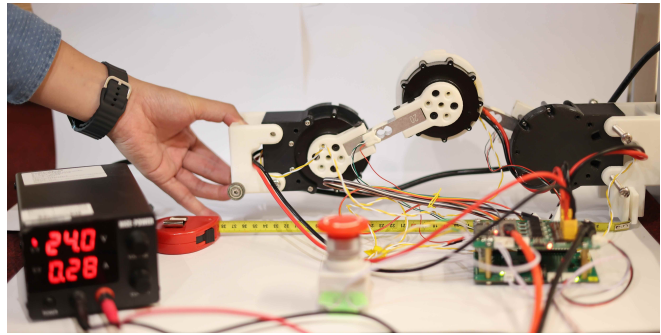


Fig. 3: Testbed of the SPARC system. One end of the spine unit is fixed, and the other (end effector) is floating to minimize friction. A horizontal force F_x is applied along the x -axis by pushing/pulling. The ruler is used to indicate the movement of the end effector, and the true displacement used for analysis is obtained from encoder-based forward kinematics.

linear-algebra operations use the Arm CMSIS-DSP library for efficient matrix solving and multiplication. With these optimizations, a single RNEA evaluation completes in approximately 17 μs on our platform, and the complete control cycle, including impedance computation, maintains the 1 kHz rate with sufficient margin for real-time operation.

IV. EXPERIMENTS AND ANALYSIS

The design objective of SPARC is to render tunable task-space compliance. We validate this through benchtop experiments that characterize: (i) static stiffness via quasi-static push-pull tests measuring force vs. displacement, and (ii) dynamic response via displacement-and-release trials under multiple damping settings. The experimental setup is shown in Fig. 3, with physical parameters in Table II.

TABLE II: Physical parameters of the spine unit

Part	Mass (kg)	Length (mm)	I_{xx}, I_{yy}, I_{zz} (kg-mm ²)
Hind spine	0.377	63.2	181, 328, 228
Hind-mid spine	0.376	117.5	148, 502, 426
Front-mid spine	0.414	117.5	991, 175, 990
Front spine	0.06	63.2	44, 92, 61

A. Static Stiffness Characterization

To validate commanded horizontal stiffness k_x , we performed quasi-static push-pull tests where a human operator manually displaced the spine end-effector along the x -axis while a load cell measured the applied force F_x . For each commanded stiffness $k_d \in \{300, 400, 500, 600, 700\}$ N/m, we conducted 10 continuous push-pull cycles. Displacement was computed from joint encoder measurements via forward kinematics.

Figure 5 shows force-displacement responses across all tested stiffness values. The measured data exhibit highly linear behavior with $R^2 \geq 0.992$ for all settings. The fitted stiffness values match commanded values within 1.5% relative error, demonstrating accurate stiffness rendering. The

system maintains linearity across the full displacement range (± 60 mm), validating the impedance control law (6).

B. Dynamic Response Characterization

To validate the damping behaviour of the controller, we recorded the step response by displacing and releasing the end effector of the spine in both the simulation and the physical platform.

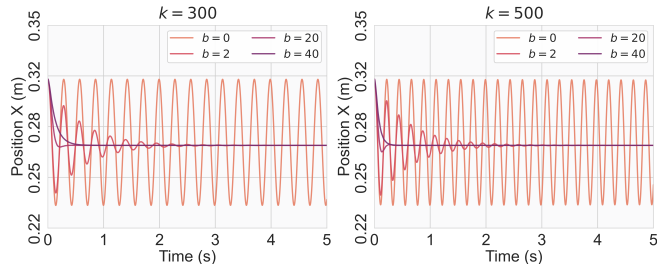


Fig. 4: Step response along x-axis of SPARC in simulation.

We tested the SPARC in MuJoCo [24], and a robot dynamics solver, BARD [25], is used for the controller implementation. A step response of the SPARC along the x-axis is recorded. In this test, we maintain the rigidity of SPARC along the z and theta axes by setting $[k_z, k_\theta] = [8000, 5]$ and $[d_z, d_\theta] = [5, 0.1]$. The spine is extended to the position $x = 0.315$ m, and the equilibrium position is set to 0.273 m. We simulated two stiffness values ($k_x \in \{300, 500\}$ N/m) with four damping coefficients ($d_x \in \{0, 2, 20, 40\}$ N·s/m) for each stiffness. As depicted in Fig. 4, a sustained oscillation can be observed when the system is undamped (i.e., $d_x = 0$). When the damping coefficient gradually increased from 2 to 40, the system transitioned from underdamped to overdamped. Also, when stiffness is increased, the natural frequency of the system increases. This evidence shows the effectiveness of our controller to mimic a spring-damper system.

In our physical test, we performed displacement-and-release tests where the end-effector was manually displaced 37 mm along the horizontal axis and then released. The system oscillation was recorded as it returned to equilibrium. The stiffness and damping coefficients are the same as those in the simulation. Each configuration was repeated 10 times.

Figure 6 shows the measured response (solid line with shaded $\pm 1\sigma$ region) compared to the ideal mass-spring-damper model (dashed line) for each parameter combination. At higher damping values ($d_x \in \{20, 40\}$ N·s/m), the measured response closely matches the ideal model. However, a small, consistent phase lag is visible. This phase deviation arises from coupling effects in the configuration-dependent task-space inertia matrix $\Lambda(x)$, which creates off-diagonal terms that couple motion directions. The effect is minor but measurable across all trials.

For the undamped case ($d_x = 0$), the controller attempts to cancel joint friction entirely using the feedforward compensation from Eq. (7). The measured response shows a slowly growing oscillation amplitude, indicating slight over-compensation. Accurate friction identification is challenging,

and even small parameter errors can result in net negative damping. This instability is limited in magnitude but demonstrates the sensitivity of friction compensation at zero commanded damping.

At low damping ($d_x = 2$ N·s/m), a different phenomenon occurs: the response gradually drifts out of phase with the ideal model as oscillations decay. This happens because joint velocities decrease with oscillation amplitude, entering the regime where Stribeck friction effects dominate. While the primary Coulomb friction coefficient was identified, secondary Stribeck parameters (Stribeck velocity v_{st} and shape parameter α in Eq. (7)) are difficult to characterize precisely. The resulting model mismatch becomes more pronounced at low velocities, causing increasing phase error as the system settles. Despite these low-speed friction artifacts, the overall damping trend matches expectations: higher commanded damping produces faster settling with less overshoot.

C. Impact of Spine Parameters on Cost of Transport

To investigate the impact of spine compliance on locomotion performance, we conducted a simulation study in MuJoCo with the SPARC-integrated quadruped. We performed a grid search over horizontal stiffness $k_x \in [500, 1500]$ N/m and damping $d_x \in [3, 25]$ N·s/m to identify parameter combinations that minimize cost of transport (CoT), defined as $CoT = E/(mgd)$, where E is the total mechanical work, m is robot mass, g is gravitational acceleration, and d is distance traveled.

Figure 7 shows the distribution of spine parameters corresponding to the top 10% lowest CoT values across two scenarios: varying terrain slope (top) and varying commanded stride length (bottom). Each subplot displays the parameter space with CoT indicated by color.

Slope effects. On downhill slopes (-11% to -1%), optimal stiffness concentrates at higher values (1000–1500 N/m) with moderate damping (5–15 N·s/m). The stiffer spine resists pitch-down during forelimb touchdown, preventing excessive forward rotation caused by gravitational acceleration. On flat terrain (-1% to 1%), optimal stiffness decreases to 800–1200 N/m. On uphill slopes (3% to 11%), optimal stiffness further decreases to 500–1000 N/m with lower damping (3–8 N·s/m). The more compliant spine enables energy storage during compression and release during extension, effectively lengthening stride against gravity.

Stride length effects. For short strides (30–60 mm), when low CoT is achieved, it occurs within a narrow stiffness range (500–600 N/m) across a wide damping span (3–25 N·s/m). This suggests that stiffness selection is more critical than damping tuning for conservative gaits. The robot operates most efficiently at moderate stride lengths (70–80 mm), where optimal parameters shift to low-to-moderate stiffness (500–800 N/m) and moderate damping (8–20 N·s/m). At these strides, the compliant spine enables effective elastic energy storage during compression and return during extension, yielding the lowest overall CoT. This parallels biological observations in dogs, which utilize a stiff-backed gallop at lower speeds but transition to a high-flexion, compliant spinal

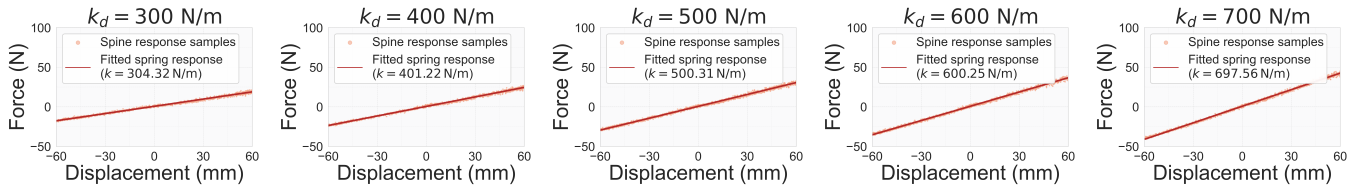


Fig. 5: Static force-displacement response for commanded $k_x \in \{300, 400, 500, 600, 700\}$ N/m. Dots show measured data; solid lines show linear fits.

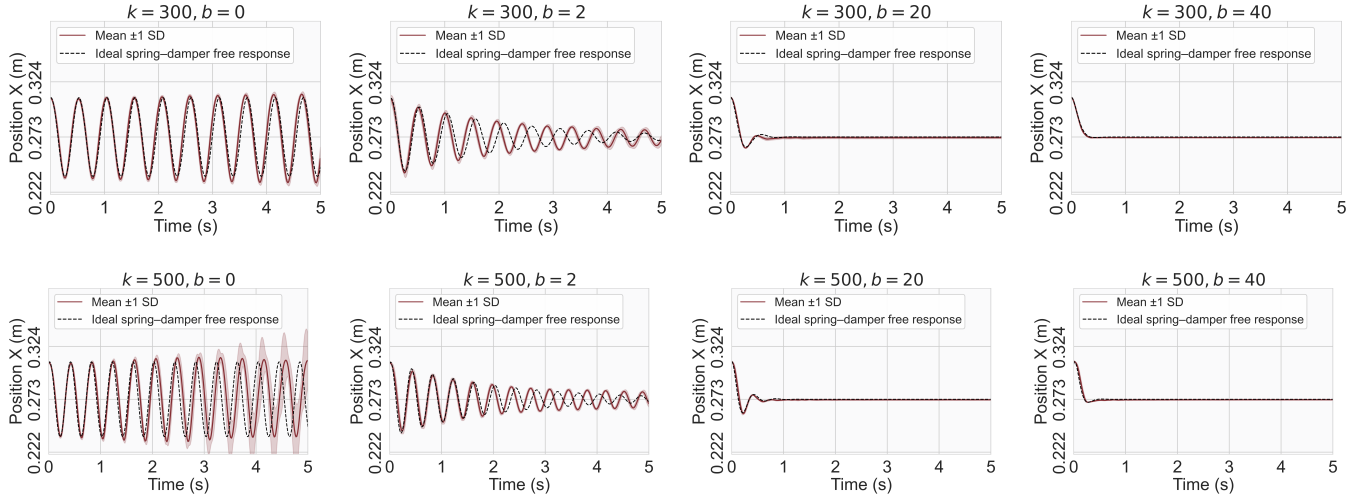


Fig. 6: Dynamic response for two stiffness values ($k_x \in \{300, 500\}$ N/m) and four damping coefficients ($d_x \in \{0, 2, 20, 40\}$ N·s/m). Measured data (solid, mean $\pm 1\sigma$) versus ideal model (dashed).

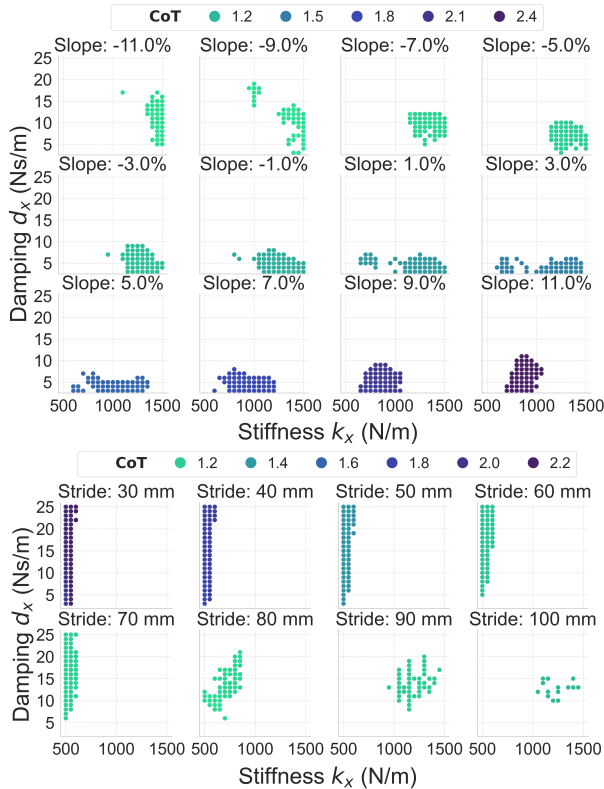


Fig. 7: Spine parameters (k_x , d_x) for the top 10% lowest CoT across varying terrain slopes (Top) and stride lengths (Bottom).

movement at maximum speeds to extend stride length and exploit elastic energy return [4]. For aggressive stride lengths (90–100 mm), optimal performance requires substantially higher stiffness (1100–1500 N/m). The stiffer spine acts as an energy transmission pathway, propagating power from the hind body to the front body during rapid take-off phases.

V. CONCLUSIONS

We have introduced SPARC, establishing a validated open-source platform for investigating 3-DoF sagittal spine compliance in quadrupedal robots. Our results confirm that the proposed impedance controller accurately renders tunable stiffness and damping without external force sensing, while simulation studies highlight that adapting these parameters to terrain slope and stride length is critical for minimizing the cost of transport. Although currently limited to benchtop characterization and simulation, this work lays the foundation for future physical integration, enabling the community to explore how active spinal flexion and extension can enhance agility and efficiency in real-world locomotion.

REFERENCES

- [1] R. M. Alexander, N. J. Dimery, and R. Ker, “Elastic structures in the back and their role in galloping in some mammals,” *Journal of zoology*, vol. 207, no. 4, pp. 467–482, 1985.
- [2] X. Zhang, C. Zhao, Z. Xu, and S. Huang, “Mechanism analysis of cheetah’s high-speed locomotion based on digital reconstruction,” *Biomimetic Intelligence and Robotics*, vol. 2, no. 1, p. 100033, 2022.
- [3] N. Schilling and R. Hackert, “Sagittal spine movements of small therian mammals during asymmetrical gaits,” *Journal of Experimental Biology*, vol. 209, no. 19, pp. 3925–3939, 2006.

- [4] J. E. Bertram and A. Gutmann, "Motions of the running horse and cheetah revisited: fundamental mechanics of the transverse and rotary gallop," *Journal of the Royal Society Interface*, vol. 6, no. 35, p. 549, 2008.
- [5] N. Kau, A. Schultz, N. Ferrante, and P. Slade, "Stanford doggo: An open-source, quasi-direct-drive quadruped," in *2019 International conference on robotics and automation (ICRA)*. IEEE, 2019, pp. 6309–6315.
- [6] B. Katz, J. Di Carlo, and S. Kim, "Mini cheetah: A platform for pushing the limits of dynamic quadruped control," in *2019 international conference on robotics and automation (ICRA)*. IEEE, 2019, pp. 6295–6301.
- [7] X. Zhang, H. Yu, B. Liu, and X. Gu, "A bio-inspired quadruped robot with a global compliant spine," in *2013 IEEE International Conference on Robotics and Biomimetics (ROBIO)*. IEEE, 2013, pp. 1312–1316.
- [8] M. Khoramshahi, A. Spröwitz, A. Tuleu, M. N. Ahmadabadi, and A. J. Ijspeert, "Benefits of an active spine supported bounding locomotion with a small compliant quadruped robot," in *2013 IEEE international conference on robotics and automation*. IEEE, 2013, pp. 3329–3334.
- [9] K. Ye, K. Chung, and K. Karydis, "A novel lockable spring-loaded prismatic spine to support agile quadrupedal locomotion," in *2023 IEEE/RSJ International Conference on Intelligent Robots and Systems (IROS)*. IEEE, 2023, pp. 2776–2783.
- [10] B. V. Beaver, *Canine behavior: a guide for veterinarians.*, 1999.
- [11] D. Chen, N. Li, H. Wang, and L. Chen, "Effect of flexible spine motion on energy efficiency in quadruped running," *Journal of Bionic Engineering*, vol. 14, no. 4, pp. 716–725, 2017.
- [12] P. Eckert, A. Spröwitz, H. Witte, and A. J. Ijspeert, "Comparing the effect of different spine and leg designs for a small bounding quadruped robot," in *2015 IEEE International Conference on Robotics and Automation (ICRA)*. IEEE, 2015, pp. 3128–3133.
- [13] J. Duperret, B. Kramer, and D. E. Koditschek, "Core actuation promotes self-manipulability on a direct-drive quadrupedal robot," in *International Symposium on Experimental Robotics*. Springer, 2016, pp. 147–159.
- [14] W. Li, Z. Zhou, and H. Cheng, "Dynamic locomotion of a quadruped robot with active spine via model predictive control," in *2023 IEEE International Conference on Robotics and Automation (ICRA)*. IEEE, 2023, pp. 1185–1191.
- [15] J. Caporale, Z. Feng, S. Rozen-Levy, A. M. Carter, and D. E. Koditschek, "Twisting spine or rigid torso: Exploring quadrupedal morphology via trajectory optimization," in *2023 IEEE International Conference on Robotics and Automation*, no. 886, 2023.
- [16] C. Fisher, S. Shield, and A. Patel, "The effect of spine morphology on rapid acceleration in quadruped robots," in *2017 IEEE/RSJ International Conference on Intelligent Robots and Systems (IROS)*. IEEE, 2017, pp. 2121–2127.
- [17] K. Ye and K. Karydis, "Modeling and trajectory optimization for standing long jumping of a quadruped with a preloaded elastic prismatic spine," in *2021 IEEE/RSJ International Conference on Intelligent Robots and Systems (IROS)*. IEEE, 2021, pp. 902–908.
- [18] S. Pouya, M. Khodabakhsh, A. Spröwitz, and A. Ijspeert, "Spinal joint compliance and actuation in a simulated bounding quadruped robot," *Autonomous Robots*, vol. 41, no. 2, pp. 437–452, 2017.
- [19] J. Di Carlo, P. M. Wensing, B. Katz, G. Bleidt, and S. Kim, "Dynamic locomotion in the mit cheetah 3 through convex model-predictive control," in *2018 IEEE/RSJ international conference on intelligent robots and systems (IROS)*. IEEE, 2018, pp. 1–9.
- [20] A. Meduri, P. Shah, J. Viereck, M. Khadiv, I. Havoutis, and L. Righetti, "Biconmp: A nonlinear model predictive control framework for whole body motion planning," *IEEE Transactions on Robotics*, vol. 39, no. 2, pp. 905–922, 2023.
- [21] R. Featherstone, *Rigid body dynamics algorithms*. Springer, 2008.
- [22] A. Albu-Schaffer, C. Ott, U. Frese, and G. Hirzinger, "Cartesian impedance control of redundant robots: Recent results with the dlr-light-weight-arms," in *2003 IEEE International conference on robotics and automation (Cat. No. 03CH37422)*, vol. 3. IEEE, 2003, pp. 3704–3709.
- [23] J. Na, Q. Chen, and X. Ren, "Chapter 1 - friction dynamics and modeling," in *Adaptive Identification and Control of Uncertain Systems with Non-smooth Dynamics*, J. Na, Q. Chen, and X. Ren, Eds. Academic Press, 2018, pp. 11–18.
- [24] E. Todorov, T. Erez, and Y. Tassa, "Mujoco: A physics engine for model-based control," in *2012 IEEE/RSJ International Conference on Intelligent Robots and Systems*. IEEE, 2012, pp. 5026–5033.
- [25] Y. Wang, "bard: Batched Articulated Robot Dynamics," Oct. 2025. [Online]. Available: <https://github.com/YueWang996/bard>